



# Temperature-induced phase and microstructural transformations in a synthesized iron carbonate (siderite) complex



Sumanta Das<sup>a,\*</sup>, Ahmet B. Kizilkanat<sup>a,b</sup>, Swaptik Chowdhury<sup>a</sup>, David Stone<sup>c</sup>, Narayanan Neithalath<sup>a</sup>

<sup>a</sup> School of Sustainable Engineering and the Built Environment, Arizona State University, Tempe, AZ, USA

<sup>b</sup> Department of Civil Engineering, Yildiz Technical University, Istanbul, Turkey

<sup>c</sup> Iron Shell LLC, Tucson, AZ, USA

## ARTICLE INFO

### Article history:

Received 15 August 2015

Received in revised form 19 November 2015

Accepted 5 December 2015

Available online 10 December 2015

### Keywords:

Iron powder

Carbonation

Thermal decomposition

Crystallization

Pore structure

Microstructure

## ABSTRACT

The influence of exposure to high temperatures on the phase transformation, microstructural features, and the resultant mechanical properties of a binder based on carbonation of metallic iron powder is reported. The extent of thermal decomposition of the binder at different temperatures is quantified using thermogravimetric analysis (TGA), whereas Fourier transform infrared (FTIR) spectroscopy and X-ray diffraction (XRD) are used for the identification of transformed phases. High temperature exposure is observed to result in stable phases, which results in the material retaining structural integrity even when exposed to 800 °C, contrary to ordinary Portland cement (OPC) pastes that degrade completely at such temperatures. Significant pore size refinement and a small reduction in porosity are noted when the pastes are exposed to high temperatures. Even though there is a significant strength loss when the iron carbonates decompose (around ~300 °C), the strengths are much higher than those of OPC pastes at higher temperatures. This provides an option for chemistry-based design of high-temperature resistant composites as well as develop structural envelope materials especially when prolonged resistance to more than 600 °C is desired.

© 2015 Elsevier Ltd. All rights reserved.

## 1. Introduction and background

Methods to reduce carbon dioxide (CO<sub>2</sub>) content in the atmosphere have resulted in several carbon capture and sequestration strategies [1–6]. Among those, mineral carbonation, especially sequestration of CO<sub>2</sub> in alkaline earth oxides, is a well-studied means [7–10]. The formation of stable minerals such as calcite, dolomite, siderite or magnesite ensures long-term chemical fixation of CO<sub>2</sub> rather than temporary storage [11–15]. It is highly beneficial from an environmental and economical viewpoint if the source material for carbonation can be a hard-to-dispose waste material, and the carbonated product can be a value-added, carbon-negative material for industrial applications. The study reported in this paper is part of such a larger effort, where chemistry-based material design is employed to produce a structural binder with properties that are comparable to or better than that of ordinary Portland cement (OPC)-based binders, from the carbonation of discarded metallic waste fines from steel shot-blasting operations. Such specialty materials, when developed and implemented for targeted applications, will ease the demand on OPC (used in concrete for building and infrastructure, and is most used material by humans after water), the production of which is energy-intensive and responsible for about 5% of the global anthropogenic CO<sub>2</sub> emissions.

Significant quantities of impure iron powder is created as bag house dust waste during the electric arc furnace (EAF) manufacturing process of steel and from the shot-blasting operations of structural steel sections. The traditional means of disposing this dust is landfilling (at great costs) as it is not economically feasible to beneficiate the powder to recover iron. A recent study, first of its kind, examined in detail, the viability of carbonating waste iron powder in an aqueous medium to produce structural binding materials [16]. The methodology was motivated by the incidences of strong and hard scale formation caused by CO<sub>2</sub>-induced corrosion in oil and gas pipelines [17–20]. The net carbonation reaction of iron powder is shown in Eq. (1) [17,21].



Even though this basic reaction scheme is thermodynamically favorable, the kinetics of reaction needs to be accelerated in order for it to be of any practical benefit. This necessitated the use of several minor ingredients as will be explained briefly here. Please refer to [16] for further details.

Waste iron powder from steel shot-blasting operations was used as the source material. In the US alone, more than 3 million tons of this material is landfilled even though a preliminary environmental impact analysis has shown that the use of virgin iron powder from processes such as electrodeposition to produce binders would still result in reduced environmental impact as compared to OPC production. The

\* Corresponding author.

E-mail address: [Sumanta.Das@asu.edu](mailto:Sumanta.Das@asu.edu) (S. Das).

parameters for ambient temperature-and-pressure synthesis of iron carbonate binder were established, including the additives needed to ensure workability, and structure-and-property development. They included a weak organic acid (oxalic acid in this case) for iron dissolution and kinetic enhancement of the reaction, fine limestone as a nucleation agent, fly ash as a silica source [16], and a kaolin clay to provide cohesiveness in the fresh state to enable handling. The sensitivity of these parameters to the carbonation efficiency and compressive strength resulted in the selection of appropriate material designs [16]. Further studies on the pore structure, microstructure [22] and mechanical response [23] were carried out to explain the enhanced performance characteristics of this material and establish it as a viable and sustainable alternative to OPC-based systems. A strong carbonate matrix and microstructural reinforcement through particulate inclusions resulted in beneficial mechanical properties.

While the aforementioned studies [16,23] established the superior mechanical performance of iron carbonate binder as compared to OPC binders at normal operating temperatures, it is important to evaluate the response of this material to elevated temperatures from the viewpoint of its chemistry and microstructure. This helps in: (i) enabling design of resilient iron carbonate-based building envelope and structural components that can better tolerate fire hazards (especially when the temperature rises to 600 °C or more as is shown in this paper), and (ii) developing high-temperature resistant, ceramic-like matrices processed at high temperatures for applications in refractory linings, solar power concentrators, and airfield pavement surfaces for military aircrafts (not an exhaustive list). It is also well known that hardened OPC paste loses its integrity and structural capacity at elevated temperatures [24–26]. Since the reaction product in the iron carbonate binder is chemically different, and there is a large amount of unreacted iron particles [22,23] that are capable of reinforcing the matrix, the high temperature response is expected to be significantly different from that of OPC-based matrices. This paper comprehensively investigates the temperature-induced chemical and microstructural transformations in this material through several advanced characterization techniques.

## 2. Experimental program

### 2.1. Materials, mixtures and specimen preparation

Metallic waste iron powder generated from a structural steel shot-blasting facility, with a median particle size of 19.03 µm, was used as the main source material in this study. The iron powder used for this study was slightly oxidized and contained approximately 90% Fe and trace amounts of Cu and Mn, as determined using particle induced X-ray emission (PIXE). Other additives such as Class F fly ash and metakaolin conforming to ASTM C 618, and limestone powder ( $d_{50}$  of 0.7 µm) conforming to ASTM C 568 were also used as minor ingredients in the binder synthesis. Table 1 provides the chemical composition of the minor ingredients along with that of the OPC. The need for these minor ingredients was explained earlier.

**Table 1**  
Chemical composition of fly ash and metakaolin used in iron carbonation, and that of OPC used for the mixtures for comparison. The limestone powder used in the iron-based binder mixtures had >95% CaCO<sub>3</sub>.

Components (%)	OPC	Fly ash	Metakaolin
SiO <sub>2</sub>	21.0	59.52	51.7
Al <sub>2</sub> O <sub>3</sub>	3.61	23.03	43.2
Fe <sub>2</sub> O <sub>3</sub>	3.47	4.62	0.5
CaO	63.0	4.87	–
MgO	3.26	–	–
SO <sub>3</sub>	3.04	0.48	–
Na <sub>2</sub> O	0.16	2.32	–
K <sub>2</sub> O	0.36	–	–
LOI	2.13	0.37	0.16

Commercially available Type I/II OPC conforming to ASTM C 150 was used to prepare OPC paste samples for comparison of performance.

The binder component used in this study includes 60% iron powder, 20% fly ash, 8% limestone, 10% metakaolin and 2% oxalic acid (all mass-based), which demonstrated the highest compressive strength and lowest porosity among a series of trial mixtures prepared as part of a detailed material design exercise [16]. The mixing procedure involves initial dry mixing of all the starting materials and then adding water to obtain a uniform cohesive mixture. A mass-based water-to-solids ratio ( $w/s$ )<sub>m</sub> of 0.24 was used to attain a cohesive mix. Since the reaction product resulting from the carbonation of iron is not a hydrate as in the case of calcium silicate hydrate (C–S–H<sup>1</sup>) gel formed in OPC systems, the role of water is mainly to ensure mass transfer and facilitate reactions. Thus a low  $w/s$ , sufficient to ensure the transport of the diffusing species in the fresh state and help molding of the specimens, is employed. Prismatic specimens of size 127 mm (length) × 25.4 mm (depth) × 25.4 mm (width) were prepared in polycarbonate molds and immediately placed inside a 100% CO<sub>2</sub> environment in room temperature. Pure CO<sub>2</sub> was circulated every 12 h so as to maintain saturation of CO<sub>2</sub> in the stored environment. After 1 day of carbonation, the specimens attained sufficient strength to sustain handling and was demolded. After demolding, the beams were placed again in the 100% CO<sub>2</sub> environment for another 5 days. After the respective duration of CO<sub>2</sub> exposure, the samples were placed in air at room temperature to allow the moisture to evaporate for further 4 days. This curing regime has been shown to result in relatively uniform product formation across the specimen depth [16,22]. Companion OPC mixtures of the same size as mentioned above were prepared with a water-to-cement ratio ( $w/c$ ) of 0.40, which is common for moderate-strength concretes used in building and infrastructure applications. The OPC beams were demolded after 1 day and were kept in a moist chamber (>98% RH and 23 ± 2 °C) for a total of 28 days. In order to investigate the effect of high temperature on OPC and iron-based binders, the specimens were heated up to 300, 600 or 800 °C in a furnace at a heating rate of approximately 5 °C/min and the target temperature was maintained for 2 h. After exposure to elevated temperatures the specimens were allowed to cool down gradually to the room temperature before being tested.

### 2.2. Thermogravimetric analysis (TGA)

A simultaneous thermal analyzer (Perkin Elmer STA 6000) was used for thermo-gravimetric analysis (TGA). The analyzer was programmed to increase the temperature from 25 °C to 995 °C at a rate of 15 °C/min in an inert N<sub>2</sub> environment. The samples for TGA were removed from a depth of 5 to 6 mm from the surface of the prismatic specimens to assess the influence of elevated temperatures on phase chemistry.

### 2.3. Mercury intrusion porosimetry (MIP)

Mercury intrusion porosimetry (MIP), which is a well-established technique to investigate the pore structure of porous materials, was adopted to study the pore structure of iron carbonate systems after exposure to different temperatures. The samples for MIP were also extracted in a similar manner as reported above for thermal analysis. The ambient temperature exposed samples were dried in an oven at 60 °C for 48 h prior to testing. MIP was performed in two steps: (i) evacuation of gases, filling the sample holder with mercury, and increasing the pressure up to 345 kPa, and (ii) intrusion of the mercury into the sample at high pressures (up to 414 MPa). The contact angle and surface tension used for the analysis were 130° and

<sup>1</sup> Typical cement chemistry notations are used here: C = CaO; S = SiO<sub>2</sub>; and H = H<sub>2</sub>O.

0.485 N/m respectively. As the contact angle between Hg and the iron carbonate phase is not known, the common value used for OPC-based pastes ( $130^\circ$ ) was used. The comparative nature of the evaluations justify the use of this value. The pore diameters can be evaluated using Washburn equation, based on the assumption that the pores are cylindrical in shape [27–29]. The total volume of mercury intruded (which is related to the porosity), and the critical pore diameter (which is the percolating pore size), are extracted from MIP. While several drawbacks of MIP for pore size determination of cementitious materials are reported [30,31], there exist consensus that the above two parameters can be accurately quantified by MIP.

#### 2.4. Fourier transform infrared spectroscopy (FTIR)

FTIR spectra for the iron-based binder sample were obtained using an ATI Mattson Genesis FTIR spectroscope with a single reflection attenuated total reflectance diamond crystal attachment. The spectra of the powders collected from a depth of 5 to 6 mm from the surface of the prismatic specimens, were obtained in the wavenumber range of 4000 to 700  $\text{cm}^{-1}$  at a resolution of 1  $\text{cm}^{-1}$ .

#### 2.5. X-ray diffraction (XRD)

XRD was performed on powdered samples using a high resolution diffractometer (PANalytical X'Pert Pro) in a  $\theta$ – $\theta$  configuration using Cu-K $\alpha$  radiation ( $\lambda = 1.54 \text{ \AA}$ ). The samples were scanned on a rotating stage between  $10^\circ$  and  $90^\circ$  ( $2\theta$ ) in a continuous mode with a step scan of  $0.05^\circ$ . A graphite monochromator was used on the primary beam, set to optimize the detection of diffracted K $\alpha$  radiation in order to minimize iron fluorescence. The powders were extracted from a depth of 5 to 6 mm from the surfaces of prismatic specimens that underwent different temperature exposures. Fine powder was used to minimize the potential for preferred orientation errors. X-ray structure information was sourced from [32].

#### 2.6. Scanning electron microscopy and electron microprobe

Microstructural analysis of the iron carbonate binders before and after high temperature exposure was carried out using a Philips XL30 field emission environmental scanning electron microscope (FESEM). Prismatic samples approximately 10 mm in size was cut from the beam samples using a diamond saw, and impregnated with epoxy resin for FESEM. A suitable combination of grinding and polishing was applied to achieve a level of flatness that ensures accurate phase identification and quantification [22]. Elemental mapping was performed using JEOL JXA-8530F Hyperprobe (electron microprobe analysis – EMPA).

#### 2.7. Determination of flexural strength using three-point bending test

The flexural strengths of both iron-based and OPC binders were determined on beams having an effective span of 101.6 mm using standard center-point loading in accordance with ASTM C 293/293M-10. The tests were performed under mid-span deflection-controlled mode. For each mixture four replicate beams were tested.

### 3. Results and discussions

#### 3.1. Evaluation of chemical transformations under high temperature exposure

This section explores temperature-induced chemical transformations in the iron carbonate binder using thermal analysis, infrared spectroscopy and XRD. These transformations have direct implications on the microstructural features and resultant properties.

#### 3.1.1. Extent of thermal decomposition of reaction product

Thermogravimetric analysis (TGA) was performed on the synthesized paste specimens at different temperatures to evaluate the stability of the different phases in the binder at elevated temperatures. Fig. 1 shows the thermogravimetric (TG) and differential TG (DTG) curves for the iron carbonate pastes exposed to different temperatures. Fig. 1(a) shows the TG/DTG curves of the iron-based binder before exposing it to any temperature regimen to determine the reaction products formed during room temperature synthesis. Note that the reaction product corresponds to a curing regime of 6 days in  $\text{CO}_2$  followed by 4 days in air. Three distinct peaks are noted in the DTG curve. The peak at around  $110^\circ\text{C}$  represents the evaporable water, the one at  $300^\circ\text{C}$  represents the thermal decomposition of iron carbonate complexed with the oxalate from the dissolution agent [16,33], and the peak at around  $750^\circ\text{C}$  is attributable to thermal decomposition of calcium carbonate added as an ingredient during the synthesis. The TG/DTG curves shown in Fig. 1(a) are used as the baseline data. It can be easily noted from Fig. 1(a)–(d) that the total mass loss decreases as the exposure temperature of the specimens is increased, with the most significant drop of about 16% when the exposure temperature is increased from ambient to  $300^\circ\text{C}$  (Fig. 1(a) and (b)). This is attributed to the loss of water as well as the thermal decomposition of the carbonate–oxalate complex [16,33]. Limestone added to the system is present in relatively unchanged amounts between both these temperatures of exposure. The quantified values of weight loss in the temperature range of  $250$ – $400^\circ\text{C}$  (corresponding to the carbonate–oxalate product and iron carbonate or siderite [34]) and the total limestone remaining in the system are reported in Table 2. It can be noted that the weight loss in the temperature range of  $250$ – $400^\circ\text{C}$  decreased from 9% at  $25^\circ\text{C}$  to about 0.14% at  $300^\circ\text{C}$  signifying almost complete decomposition of iron carbonate complex when the paste is heated to  $300^\circ\text{C}$ . At  $300^\circ\text{C}$ , the calcite peak is still present as calcite decarbonates only at higher temperatures.

For the paste exposed to  $600^\circ\text{C}$  (Fig. 1(c)), the peak at around  $750^\circ\text{C}$  corresponding to the thermal decomposition of calcite reduced significantly in intensity, implying almost complete decomposition of calcite. It should be noted that pure calcite exhibits its maximum rate of thermal decomposition at around  $730$ – $750^\circ\text{C}$  although the process occurs in the  $600$ – $850^\circ\text{C}$  range especially when organic acids are used as additives [35,36]. Table 2 shows that only trace amounts of calcite (0.07%) remain in the system when the sample was exposed to  $600^\circ\text{C}$  for 2 h. The combination of the increased exposure duration and the presence of oxalic acid (added to facilitate iron dissolution) which decreases the energy consumption during the decomposition process are responsible for this observation. When exposed to  $800^\circ\text{C}$ , the original components present are found to be almost totally decomposed. However, visual inspection of the prismatic samples even after exposure to  $800^\circ\text{C}$  revealed a compact, dense, and undamaged structure (shown later in the paper). This points to the fact that other temperature-resistant (at least up to  $995^\circ\text{C}$  which was the upper limit of the TG experiments) chemical species would have formed in these systems as a result of high-temperature exposure, which is examined using XRD in a later section.

The FTIR spectra of powdered samples of pastes subjected to different exposure temperatures are shown in Fig. 2. Overall, three distinct peaks are observed in the spectra at ambient temperature. The peak in the wavenumber range of  $1410$  to  $1425 \text{ cm}^{-1}$  represents stretching vibration of the carbonate (C–O) bond whereas the peak in the  $860$  to  $880 \text{ cm}^{-1}$  range represents out-of-plane bending of the C–O bond [37, 38]. The peak in the  $930$  to  $1060 \text{ cm}^{-1}$  range represents the asymmetric stretching vibration of Si–O–Si bond [37–39]. The stretching and out-of-plane bending vibrations of the C–O bond indicates the presence of iron carbonate and calcite even though precise identification of corresponding species requires spectral deconvolution [40], which is not carried out in this study. However, it has been reported that the peak at  $860 \text{ cm}^{-1}$  can be attributed to siderite [41], which is strongly observed in the specimen exposed to ambient temperature. The broadness of the

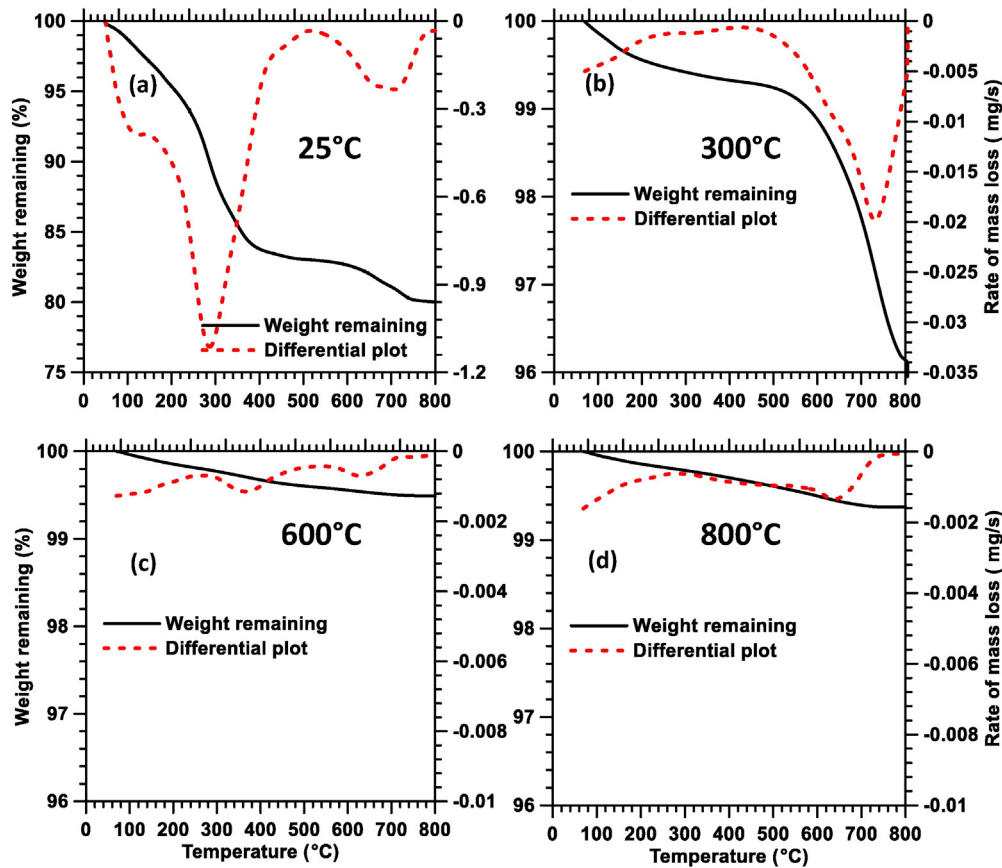


Fig. 1. TG and DTG curves for iron-based binder samples exposed to: (a) 25 °C; (b) 300 °C; (c) 600 °C; and (d) 800 °C. Note that the TG and DTG axes are not the same between all the specimens.

peak corresponding to asymmetric stretching vibration of Si–O–Si indicates the presence of structural disorder in the silicate network and thus, the likely amorphous nature of silicates present in this system at ambient temperatures [37,42].

When the pastes are exposed to 300 °C, the intensities of the C–O peaks (at 1424 and 875  $\text{cm}^{-1}$ ) relative to the silicate peak (at 1048  $\text{cm}^{-1}$ ) are reduced which can be attributed to the near-complete thermal decomposition of the iron carbonate reaction product as confirmed by TG/DTG results in the previous section. Thus the C–O peaks in this sample conditioned at this temperature are attributed almost entirely to calcium carbonate, which is also supported by the increased sharpness of the peak. The broad silicate peak corresponding to amorphous silica is still present at this exposure temperature. Increasing the exposure temperature to 600 °C results in the disappearance of the C–O peaks due to decarbonation, which is also in line with the TG/DTG results. In addition, the silicate peak width reduces considerably and the peak shifts to lower wave numbers as compared to the specimens exposed to lower temperatures. This is an indication of the change in structural arrangement of the product when exposed to higher temperatures. The Si–O–Si peak width is further reduced when the exposure temperature was increased to 800 °C denoting the presence of more polymerized silicate species. It is also likely that complex silicates containing iron and calcium (from the decomposition of

calcite) could have formed at high exposure temperatures, but their presence could not be accurately confirmed from the FTIR spectra shown here, except for the fact that the widths reduce and intensities increase for the Si–O–Si stretching vibration. Later on in this paper, we demonstrate the likely presence of such a phase using electron microprobe analysis. The crystalline phases formed at high temperature, especially the iron bearing ones such as hematite and magnetite, generally show characteristic peaks at much lower wavenumbers (550–600  $\text{cm}^{-1}$ ) [43] which were not detected using FTIR spectroscopy

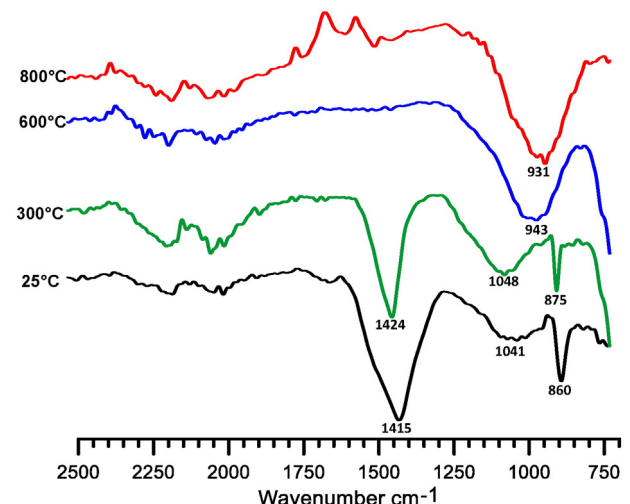


Fig. 2. FTIR spectra for the iron-based binder pastes exposed to different temperatures.

Table 2

Quantitative results from thermal analysis as a function of exposure temperature.

Weight loss from 250 to 400 °C (% of initial mass)				Calcite remaining (% of initial mass)			
25 °C	300 °C	600 °C	800 °C	25 °C	300 °C	600 °C	800 °C
9.05	0.14	0.15	0.04	4.85	4.841	0.07	0.05

in this study. Hence, in an effort to monitor the evolution of the crystalline species, XRD is used, as presented in the following section.

### 3.1.2. XRD for phase analysis at elevated temperatures

XRD was carried out on powdered paste samples subjected to the chosen temperatures. Fig. 3 shows the XRD spectra of iron-based binders after being subjected to all the four exposure temperatures studied here. At room temperature, siderite, which is an iron carbonate mineral, is found predominantly, as expected. In addition, peaks corresponding to calcite (accounting for the limestone added), quartz (from fly ash), and magnetite ( $\text{Fe}_3\text{O}_4$ ; potentially oxidized iron particles from the source material) are also present. When the specimens were exposed to a temperature of 300 °C for 2 h, iron carbonate decomposes in the presence of oxygen to form magnetite ( $\text{Fe}_3\text{O}_4$ ) as shown in Eq. (2) [44,45]. The magnetite further oxidizes to  $\gamma\text{-Fe}_2\text{O}_3$  [45,46] as shown in Eq. (3).



The above oxidation reactions are thermodynamically favorable at temperatures greater than 200 °C [45,46]. This is the reason for both  $\text{Fe}_3\text{O}_4$  and  $\gamma\text{-Fe}_2\text{O}_3$  being present in the XRD spectrum of the paste exposed to 300 °C. The peak corresponding to calcite is also detected in the XRD spectrum for the specimen exposed to 300 °C, which is in line with the TGA results presented in the previous section. Beyond an exposure temperature of 400 °C,  $\gamma\text{-Fe}_2\text{O}_3$  (maghemite) is further oxidized to  $\alpha\text{-Fe}_2\text{O}_3$  or hematite. In addition, at temperatures above 575 °C magnetite is also directly oxidized to form hematite [46].



The samples from the specimen exposed to 600 °C are primarily composed of magnetite and hematite as observed from the XRD spectrum. Both magnetite and hematite are crystalline in nature and this impacts the properties of the material when the exposure temperature is increased, as will be explored in a forthcoming section. The powder from the specimen exposed to 800 °C also shows both magnetite and

hematite in the XRD spectra. However, the number of peaks corresponding to hematite is higher in the sample exposed to 800 °C as compared to that at lower temperatures, suggesting an increase in crystallinity of these products with increasing temperature of exposure. The XRD spectra for the sample exposed to 800 °C matches well with that of  $\alpha\text{-Fe}_2\text{O}_3$  nanoparticles (hematite) [47]. These iron oxides, especially hematite, formed after high-temperature exposure, are considered to be among the most stable minerals on earth's surface [48,49]. Chemical leaching tests have also established in the durability of these minerals [48]. An increase in number of peaks corresponding to quartz at 800 °C also points to the polymerization of free silica at elevated temperature. Another interesting finding is that the full width at half maximum (FWHM) of the XRD peaks corresponding to  $\text{Fe}_3\text{O}_4$  and  $\text{Fe}_2\text{O}_3$  reduces as the temperature is increased from 300 °C to 800 °C, which also indicates a significantly higher crystallinity at higher temperatures. The overall amorphous content reduces significantly when the specimen is exposed to 800 °C. The above factors influence the mechanical behavior of the material – the higher crystallinity and chemical stability of the high-temperature reaction products likely negating to a certain extent, the loss in properties at intermediate temperatures when the iron carbonate reaction product decomposed. The microstructural study provided in the following section provides further insights into this behavior.

### 3.2. Microstructural effects of high-temperature exposure

#### 3.2.1. Influence of temperature-induced phase transformation on the pore structure

Temperature-induced decomposition and transformation of phases will result in changes in the pore structure and microstructure of the material, thereby directly impacting its engineering properties. Fig. 4(a) shows representative total volume intruded and differential volume curves obtained from MIP studies. The dominant peak in the differential curve indicates the percolating (threshold) pore size which dictates the moisture-and-ionic transport induced material durability issues. Fig. 4(b) shows that the total porosity more than doubles when the exposure temperature was increased from ambient to 300 °C. This must be viewed in conjunction with the TG/DTG results shown earlier where the decomposition of the iron carbonate complex was shown to happen at around 300 °C. The major binding material is decomposed, creating a large porosity in the specimen. Between exposure temperatures of 300 and 600 °C, there is no appreciable change in porosity. Even though calcite decomposition occurs in this temperature range as explained earlier, the XRD spectrum indicates the formation of other iron-bearing phases, which likely compensates the calcite loss. A further increase in exposure temperature to 800 °C results in the porosity being reduced slightly.

The critical pore sizes presented in Fig. 4(b) reveal more information on the influence of temperature on the pore structure. Between exposure temperatures of 25 and 300 °C, the critical pore diameter increases slightly, but the increase is not commensurate with the increase in porosity. Beyond 300 °C, further increase in exposure temperature results in considerable reduction in the critical pore sizes even though the porosities are rather invariant. This indicates that the phase transformations occurring as a result of high temperature exposure, confirmed by the XRD spectra, results in the formation of a microstructure with smaller pore sizes. In order to quantify the pore size refinement as a function of exposure temperature, the pores are classified into three ranges<sup>2</sup>: (i) 0.0035 to 0.05  $\mu\text{m}$ , (ii) 0.05 to 0.2  $\mu\text{m}$  and (iii) >0.2  $\mu\text{m}$  at different temperatures shown in Fig. 4(c). This classification is generally in line

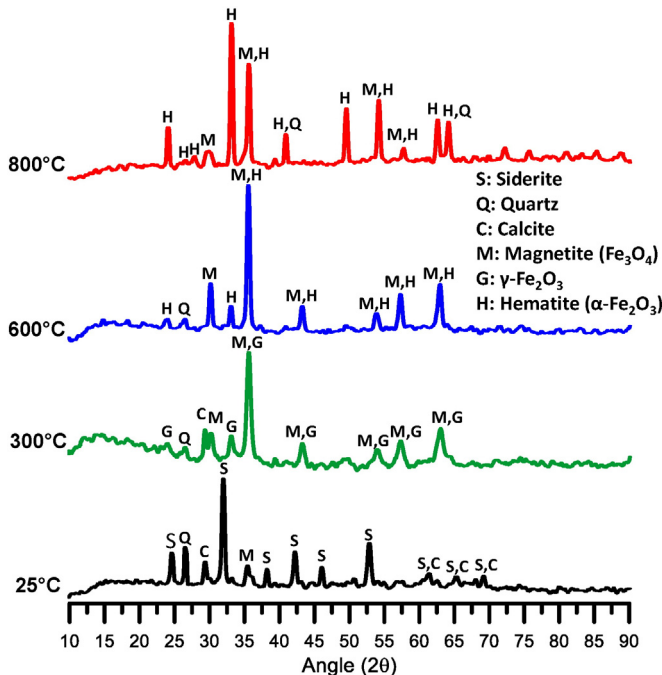
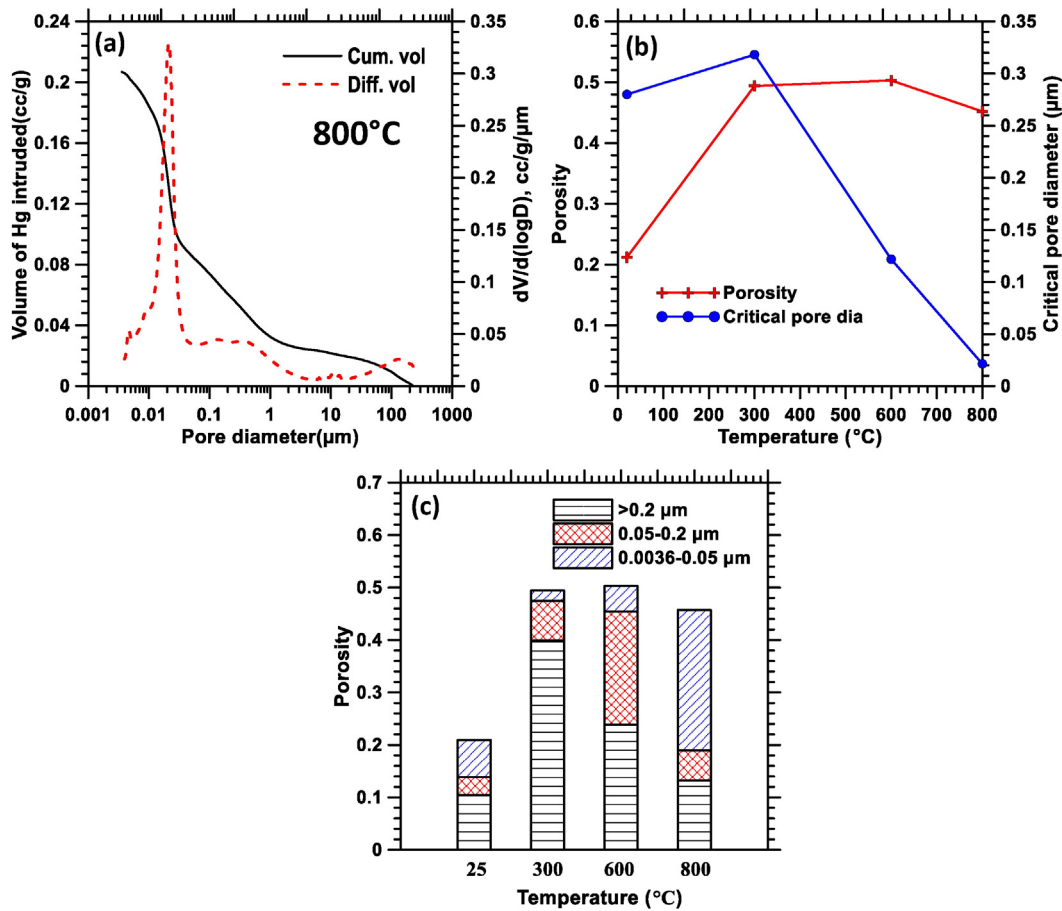


Fig. 3. XRD spectra for the iron carbonate binders exposed to different temperatures.

<sup>2</sup> MIP is well-known to be a technique that has issues when it comes to the pore size determination, primarily because of the ink-bottle effect [31]. However, this study uses the pore size distribution only to compare among mixtures that are relatively similar, which makes this method acceptable.



**Fig. 4.** (a) Representative volume intruded and differential volume curves from MIP, (b) the influence of exposure temperature on the porosity and critical pore size, and (c) distribution of pore sizes as a function of exposure temperature.

with that of the IUPAC recommendation [50]. The fraction of larger pores ( $>0.2 \mu\text{m}$ ) increases significantly when the exposure temperature is increased from  $25^{\circ}\text{C}$  to  $300^{\circ}\text{C}$ , attributed to the thermal decomposition of iron carbonate as explained before. This results in an increase in the porosity also. Increasing the exposure temperature to  $600^{\circ}\text{C}$  reduces the fraction of bigger pores ( $>0.2 \mu\text{m}$ ) and increases the fraction of smaller pores significantly, suggesting a fundamental change in the reaction product as was demonstrated by XRD. Most of the larger pores are found to be transformed to pores of intermediate size ( $0.05\text{--}0.2 \mu\text{m}$ ). At  $800^{\circ}\text{C}$ , the dominant fraction of porosity is contributed by the smallest pores ( $0.0036\text{--}0.05 \mu\text{m}$ ) due to predominance of crystalline hematite in the material structure as revealed by XRD. The results shown here indicate a sequential refinement of pore sizes (not much of a reduction in porosity) as the exposure temperature is increased from  $300^{\circ}\text{C}$  to  $800^{\circ}\text{C}$ , pointing to changes in structural order and formation of crystalline phases, which are confirmed through XRD.

### 3.2.2. Influence of exposure temperature on the microstructure

Fig. 5 shows micrographs of the iron-based binder after exposure to different temperatures. The bright particles seen in the micrographs correspond to the iron particles. Denser reaction product formation around unreacted angular iron particles is distinctively visible in Fig. 5(a) that corresponds to an exposure temperature of  $25^{\circ}\text{C}$ . While the carbonate reaction product binds the unreacted iron particles and provides overall strength to the composite material, the unreacted iron particles facilitate microstructural reinforcement that enhances the mechanical properties of the material when compared to conventional cement-based systems [23]. When the binder is exposed to  $300^{\circ}\text{C}$ , the denser light gray phases around

the unreacted iron particles corresponding to the carbonate reaction products are converted to darker, low-density phases as can be noticed from Fig. 5(b). This is attributed to the thermal decomposition of iron carbonate as was confirmed through TGA and XRD results shown in the preceding sections. From a microstructural perspective, as observed from electron micrographs, there are no significant morphological changes between exposure temperatures of  $300$  and  $600^{\circ}\text{C}$  (Fig. 5(b) and (c)), to go along with the unchanged porosity as shown in Fig. 4(b). However XRD indicated phase transformations, which are not identified in the micrographs. Some of the darker phases around the iron particles observed in the micrographs of specimens exposed to  $300^{\circ}\text{C}$  and  $600^{\circ}\text{C}$  are absent in the micrograph of the specimen exposed to  $800^{\circ}\text{C}$  as observed in Fig. 5(d). This likely indicates significant differences in reaction products when the specimens are exposed to a higher temperature, as indicated by the other techniques described earlier. While the microstructures shown here demonstrate some degree of matrix damage, especially at  $300$  and  $600^{\circ}\text{C}$ , morphological changes are not adequately captured by backscattered SEM images.

Fig. 6 shows the elemental maps obtained using electron microprobe analysis (EMPA) coupled with energy dispersive X-ray spectra (EDS) of the samples exposed to different temperatures. The parent micrographs at three chosen exposure temperatures are shown along with the elemental maps corresponding to Fe, C, Si, and Ca. At room temperature (Fig. 6(a)), the presence of Fe as both unreacted iron particles (bright phase in the micrographs) and dispersed throughout the microstructure are observed. Carbon is well distributed in the microstructure, both as iron carbonates and unreacted limestone. The added fly ash and metakaolin demonstrate discrete pockets of silica

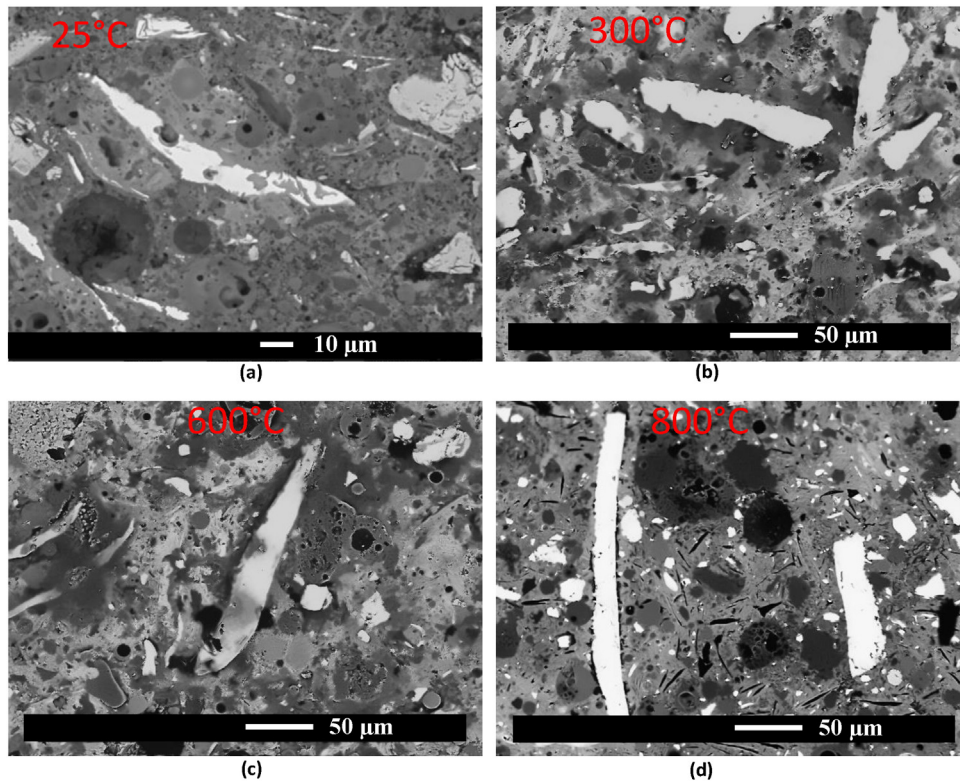


**Fig. 5.** Evolution of microstructure as a function of the exposure temperature: (a) 25 °C; (b) 300 °C; (c) 600 °C; and (d) 800 °C. The exposure duration at all the non-ambient temperatures was 2 h.

in the microstructure while calcium is observed, again as a distributed element, owing to the presence of fly ash and limestone. When the exposure temperature was increased to 300 °C (Fig. 6(b)), iron carbonates are decomposed as evidenced by the thermal analysis results, which is revealed in the C elemental map as dark zones around the iron particles since the concentration of iron carbonate is highest in the proximity of the iron particles. In these dark zones around the iron particles (see the parent micrograph), the concentration of Si is observed to be high, since the decomposition of iron carbonates result in the continuous matrix connecting the unreacted iron particles being mostly composed of fly ash and metakaolin, both of which are silica-rich (>50% of SiO<sub>2</sub> by mass – Table 1). Calcite, which is the dominant Ca source in the microstructure, is unaffected at this temperature, as seen from the Ca elemental maps at both 25 °C and 300 °C.

The elemental maps for the specimens exposed to 800 °C are shown in Fig. 6(c). The most important observation is that most of the C has disappeared from the microstructure, pointing to the decomposition of all the carbonates in the system. The material, realistically, thus is no more a carbonate when exposed to higher temperatures. It is a heterogeneous material chemically composed of magnetite, hematite, and quartz as demonstrated by XRD, coupled with other X-ray amorphous phases. More diffuse spread of iron is noticed in the elemental map, along with that of Si. Rounded, silica-rich fly ash particles are present along with diffuse silica in the microstructure. The elemental map of Ca shows a significant difference from those at lower exposure temperatures. At 800 °C, Ca is diffused uniformly through the microstructure, and is present everywhere except in the locations of the unreacted iron particles. This is an indication of the likely formation of calcium–ferrite complexes where hematite, found in the XRD trace at 600 °C, engages in solid-state reactions at around 750–780 °C with CaO formed from limestone decomposition [51]. More studies on the phase structure and compositions after high-temperature exposure are needed.

### 3.3. Implications of temperature-induced chemical/microstructural transformations on the mechanical behavior

The foregoing sections have provided a detailed understanding of the influence of elevated temperature on the reaction products and microstructure of iron-based binder systems. This section explores the implications of temperature-induced chemical and microstructural changes on the mechanical strength of this binder system, in order to establish the application scenarios listed in the introduction section. Fig. 7(a) presents the flexural strengths as a function of exposure temperature along with those of OPC pastes for comparison. At room temperature, the iron-based binder exhibits a significantly higher (by about 6 times) flexural strength as compared to the OPC paste, the reasons for which are explored in detail elsewhere [16,23]. Thermally aided decomposition of iron carbonate, confirmed through TGA/XRD, and subsequent increase in porosity when exposed to 300 °C are reflected here in the form of significant reduction in flexural strength. It also points to the fact that iron carbonate is the main reaction product in this binder system that facilitates binding of all the other unreacted/inert materials.

A comparison of the performance of the two binder systems when exposed to 300 °C reveals that the iron-based binder suffers a major loss in strength (about 80% of its initial strength) whereas OPC gains strength attributed to: (i) enhanced reaction occurring under high temperatures before the moisture is removed, that results in some pore filling, and (ii) removal of the moisture from the pores and a consequent apparent strength increase [52,53]. However, iron-based binder is almost as strong as OPC at 300 °C due to its significantly higher strength at room temperature. This loss in strength at 300 °C of the iron-based binder is also reflected in the form of a 20% reduction in bulk density, shown in Fig. 7(b). When exposed to 600 °C, the flexural strength increases slightly for the iron-based binder whereas the OPC paste loses its strength by more than 40%

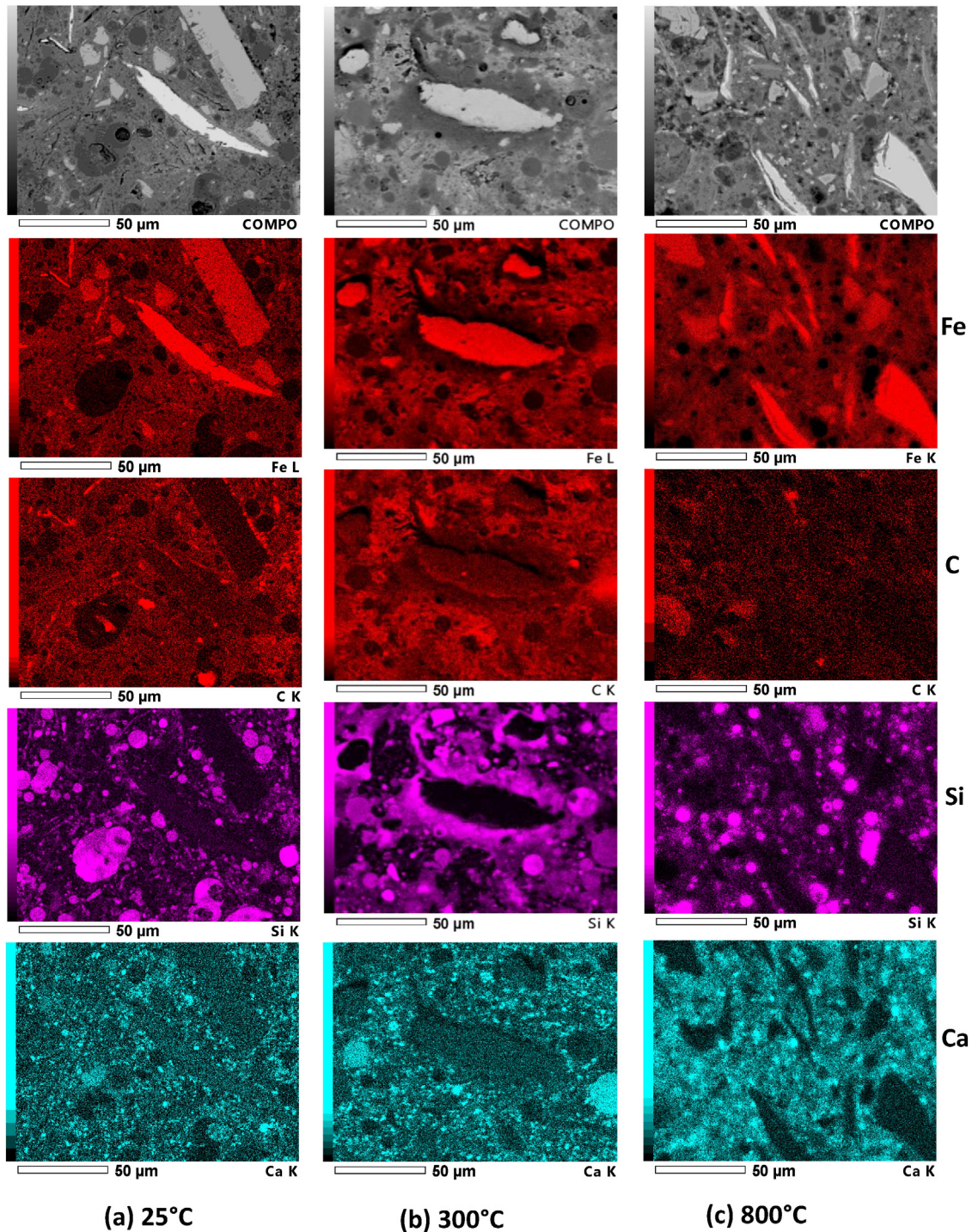


**Fig. 6.** Elemental maps of the microstructure obtained using electron microprobe analysis (EMPA) for specimens exposed to different temperatures. (a) 25 °C; (b) 300 °C; and (c) 800 °C. EMPA corresponding to Fe, C, Si, and Ca are shown here.

as compared to its strength at 300 °C. The strength loss of the OPC binder can be attributed to the decomposition of calcium hydroxide (CH) at around 450 °C and the subsequent increase in porosity [54]. On the other hand, a slight increase in the strength of the iron-based binder can be attributed to the onset of temperature-induced crystallization process as explored in the previous sections. When exposed to 800 °C, the flexural strength of the iron-based binder is found to increase significantly (by ~65% as compared to that at 600 °C) whereas OPC has lost almost all its strength because of the total decomposition of the calcium silicate hydrate (C-S-H) gel [55]. The significant increase in strength for the iron-based binder is the result

of increase in crystallinity and formation of denser structure at 800 °C as discussed earlier. Fig. 7(c) shows the strength–porosity relationship of the iron-based binder.

Fig. 8 shows the visual appearance of OPC and the iron carbonate paste beams subjected to different temperatures. Fig. 8(a-1 to d-1) shows the sequential temperature-induced degradation of OPC matrix whereas Fig. 8(a-2 to d-2) shows the changes in appearance of the iron-based matrix. Cracks develop in OPC pastes beyond 150–200 °C because of shrinkage stresses and the cracks can be seen visually in the paste exposed to 300 °C (Fig. 8(b-1)). A few cracks are also noticed in the iron carbonate paste (Fig. 8(b-2)) exposed to 300 °C due to the

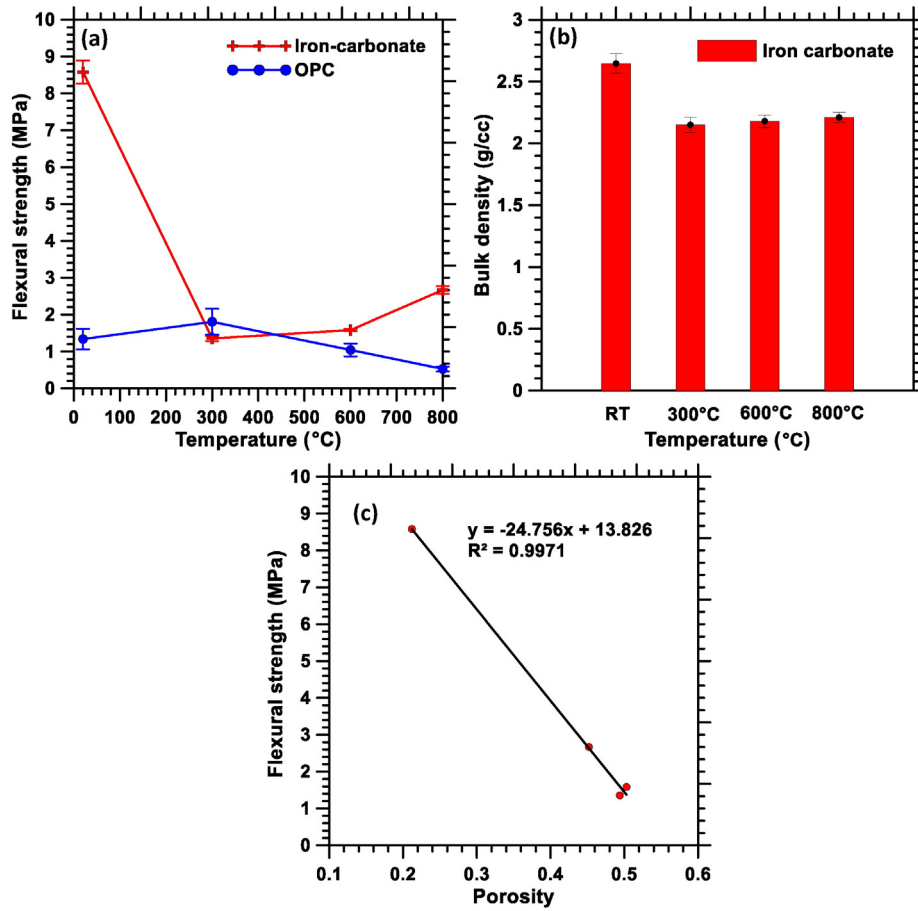


Fig. 7. (a) Flexural strengths of the iron-based binder and its comparison to traditional OPC pastes, as a function of temperature; (b) bulk density of iron-based binder as a function of exposure temperature, and (c) flexural strength–porosity relationship for the iron-based binder.

stresses induced by the thermal decomposition of iron carbonate. At approximately 600 °C, the width of the cracks increases significantly in the OPC paste sample (Fig. 8(c-1)) resulting in significant loss of strength (Fig. 7(a)). Also, explosive spalling is reported to occur in this temperature range, which reduces the integrity and load bearing capacity

substantially [56]. While cracks in hardened cement paste become wider with associated significant strength deterioration at 600 °C, the cracks formed in the iron carbonate sample at 300 °C gets healed to a large extent as the temperature is increased to 600 °C which is a consequence of temperature-induced phase-transformation of reaction

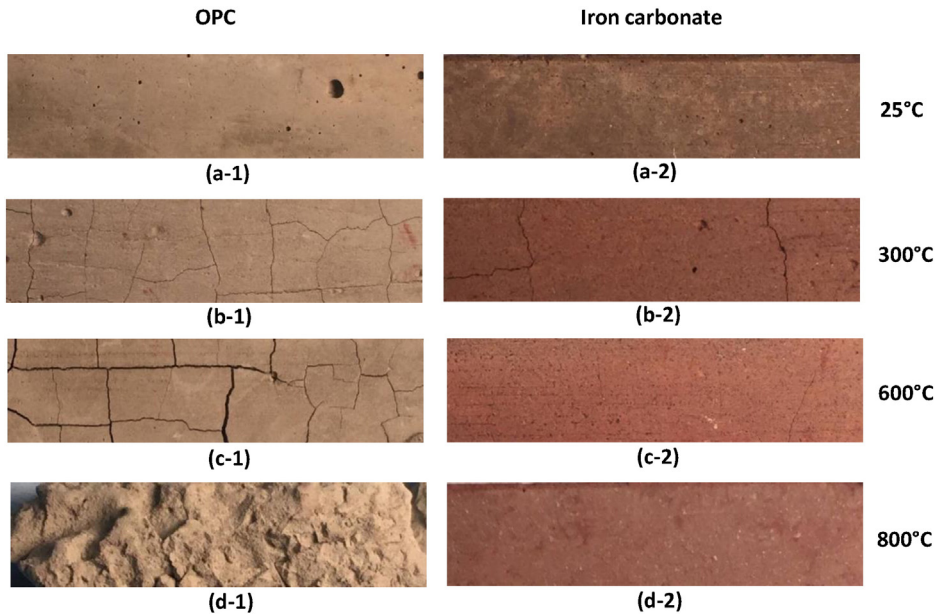


Fig. 8. Visual appearance of OPC (a) and iron carbonate (b) paste samples (50 mm × 12.5 mm × 12.5 mm) at different temperatures: (a) 25 °C; (b) 300 °C; (c) 600 °C, and (d) 800 °C.

products into crystalline phases such as hematite and magnetite. The OPC paste sample is severely degraded with loss of structural integrity before 800 °C as shown in Fig. 8(d-1). On the contrary, the iron-based binder shows a smooth and stable surface with no apparent discontinuities. The structural integrity is maintained (or regained) along with strength enhancement (as compared to that at 300 °C) when exposed to higher temperatures. The reaction products found in the iron-based binder at this temperature are high-temperature stable phases and thus it is expected that even further temperature increase does not compromise the structural integrity or reduce the strength. This aspect enables the development of effective high-temperature resistant composites without the use of expensive starting materials. Treatment of this room-temperature processed material to 800 °C results in a robust high-temperature resistant material that can be used in solar energy applications, and as vertical landing/takeoff pads or military aircrafts. The material also becomes a viable candidate for envelope or structural systems that are likely to encounter fires that burn to 600 °C or more.

#### 4. Summary and conclusions

The influence of temperature on phase transformations and the resultant microstructure and mechanical properties of an iron-based binder system was explored in this paper. Thermal analysis of specimens subjected to different temperatures showed that the iron carbonate complex decomposed at 300 °C, while calcite mostly decomposed when exposed to 600 °C for 2 h. FTIR spectra also confirmed the decomposition of carbonates through the disappearance of the C–O peaks when exposed to higher temperatures. At higher exposure temperatures, the width of the Si–O–Si peak reduced, denoting the presence of more polymerized silicate species. XRD revealed aspects of phase transformation that could not be revealed through thermal and spectroscopic analysis. The formation of stable magnetite and hematite phases when iron carbonates were exposed to high temperatures were observed.

MIP and SEM were used to understand the microstructural changes resulting from high temperature exposure of the iron-based binder. The porosity increased significantly when the exposure temperature was increased to 300 °C attributed to the loss of the main binding material, iron carbonate. Further increase in temperature resulted in slight reduction in porosities, attributed to the formation of stable phases. Increasing exposure temperature resulted in pore size refinement, exemplified by the critical pore sizes being lower by more than 7 times and the proportion of finer pores (0.0035 to 0.05 µm) increasing tenfold, between exposure temperatures of 300 °C and 800 °C. Elemental maps coupled with electron micrographs indicated the distribution of different elements (Fe, C, Si, Ca) in the microstructure as a function of exposure temperature – C disappearing gradually between 300 °C and 800 °C, Fe becoming more diffused, and Ca spreading more uniformly at 800 °C, likely indicating the presence of a calcium–ferrite complex.

The influence of the chemical phase transformations and resultant microstructural changes on the flexural strengths was determined. The reduction in strength followed the trend of increase in porosity, as is common with porous materials. While the iron-based binder lost significant amounts of strength by 300 °C, there was some strength improvement when the exposure temperature was increased. When exposed to 800 °C, the iron-based binder had a strength that was more than thrice of that of OPC pastes, and more importantly, the integrity of the material was uncompromised, contrary to OPC-based systems. These results demonstrated that this material when processed at high temperatures, could serve as high-temperature resistant composites, and as envelope or structural systems that require resistance to temperatures in excess of 600 °C, where OPC-based systems cannot effectively function.

#### Acknowledgments

The authors sincerely acknowledge the support from the National Science Foundation (CMMI: 1463646) towards the conduct of this study. The second author acknowledges the Scientific and Technological Research Council of Turkey (TUBITAK) for financial support. The contents of this paper reflect the views of the authors who are responsible for the facts and accuracy of the data presented herein, and do not necessarily reflect the views and policies of NSF, nor do the contents constitute a standard, specification or a regulation. We gratefully acknowledge the support that has enabled the establishment of the Laboratory for the Science of Sustainable Infrastructural Materials (LS-SIM) at Arizona State University. XRD and SEM/EMPA were carried out at the LeRoy Eyring Center for Solid State Sciences at ASU, which is acknowledged. Raw materials were provided by Schuff Steel, Iron Shell LLC, Omya AG, Headwaters Inc., and Burgess Pigments, which are also acknowledged.

#### References

- [1] M.R. Liebl, J. Senker, Microporous functionalized triazine-based polyimides with high CO<sub>2</sub> capture capacity, *Chem. Mater.* 25 (2013) 970–980.
- [2] M.G. Rabbani, H.M. El-Kaderi, Template-free synthesis of a highly porous benzimidazole-linked polymer for CO<sub>2</sub> capture and H<sub>2</sub> storage, *Chem. Mater.* 23 (2011) 1650–1653.
- [3] H.A. Patel, D. Ko, C.T. Yavuz, Nanoporous benzoxazole networks by silylated monomers, their exceptional thermal stability, and carbon dioxide capture capacity, *Chem. Mater.* 26 (2014) 6729–6733.
- [4] G. Bhattacharjee, A. Kumar, T. Sakpal, R. Kumar, Carbon dioxide sequestration: influence of porous media on hydrate formation kinetics, *ACS Sustainable Chem. Eng.* 3 (2015) 1205–1214.
- [5] H. Kweon, C. Payne, M. Deo, Reactive and pore structure changes in carbon dioxide sequestration, *Ind. Eng. Chem. Res.* 54 (2015) 4552–4560.
- [6] D.N. Huntzinger, J.S. Gierke, S.K. Kawatra, T.C. Eisele, L.L. Sutter, Carbon dioxide sequestration in cement kiln dust through mineral carbonation, *Environ. Sci. Technol.* 43 (2009) 1986–1992.
- [7] E. Klein, M. De Lucia, T. Kempka, M. Kühn, Evaluation of long-term mineral trapping at the Ketzin pilot site for CO<sub>2</sub> storage: an integrative approach using geochemical modelling and reservoir simulation, *Int. J. Greenh. Gas Control* 19 (2013) 720–730.
- [8] T. Xu, J.A. Apps, K. Pruess, Numerical simulation of CO<sub>2</sub> disposal by mineral trapping in deep aquifers, *Appl. Geochem.* 19 (2004) 917–936.
- [9] T. Naganuma, K. Yukimura, N. Todaka, S. Ajima, Concept and experimental study for a new enhanced mineral trapping system by means of microbially mediated processes, *Energy Procedia* 4 (2011) 5079–5084.
- [10] O. Qafoku, L. Kovarik, R.K. Kukkadapu, E.S. Ilton, B.W. Arey, J. Tucek, et al., Fayalite dissolution and siderite formation in water-saturated supercritical CO<sub>2</sub>, *Chem. Geol.* 332–333 (2012) 124–135.
- [11] E.H. Oelkers, S.R. Gislason, J. Matter, Mineral carbonation of CO<sub>2</sub>, *Elements* 4 (2008) 333–337.
- [12] P.B. Kelemen, J. Matter, In situ carbonation of peridotite for CO<sub>2</sub> storage, *Proc. Natl. Acad. Sci.* 105 (2008) 17295–17300.
- [13] O.S. Pokrovsky, S.V. Golubev, J. Schott, Dissolution kinetics of calcite, dolomite and magnesite at 25 °C and 0 to 50 atm pCO<sub>2</sub>, *Chem. Geol.* 217 (2005) 239–255.
- [14] T. Xu, J.A. Apps, K. Pruess, Mineral sequestration of carbon dioxide in a sandstone–shale system, *Chem. Geol.* 217 (2005) 295–318.
- [15] K. Dideriksen, C. Frandsen, N. Bovet, A.F. Wallace, O. Sel, T. Arbour, et al., Formation and transformation of a short range ordered iron carbonate precursor, *Geochim. Cosmochim. Acta* 164 (2015) 94–109.
- [16] S. Das, B. Souliman, D. Stone, N. Neithalath, Synthesis and properties of a novel structural binder utilizing the chemistry of iron carbonation, *ACS Appl. Mater. Interfaces* 6 (2014) 8295–8304.
- [17] M.B. Kermani, A. Morshed, Carbon dioxide corrosion in oil and gas production – a compendium, *Corrosion* 59 (2003) 659–683.
- [18] S.L. Wu, Z.D. Cui, F. He, Z.Q. Bai, S.L. Zhu, X.J. Yang, Characterization of the surface film formed from carbon dioxide corrosion on N80 steel, *Mater. Lett.* 58 (2004) 1076–1081.
- [19] M. Nordsveen, S. Nešić, R. Nyborg, A. Stangeland, A mechanistic model for carbon dioxide corrosion of mild steel in the presence of protective iron carbonate films—part 1: theory and verification, *Corrosion* 59 (2003) 443–456.
- [20] S. Nesić, J. Postlethwaite, S. Olsen, An electrochemical model for prediction of corrosion of mild steel in aqueous carbon dioxide solutions, *Corrosion* 52 (1996) 280–294.
- [21] J.B. Sun, G.A. Zhang, W. Liu, M.X. Lu, The formation mechanism of corrosion scale and electrochemical characteristic of low alloy steel in carbon dioxide-saturated solution, *Corros. Sci.* 57 (2012) 131–138.
- [22] S. Das, D. Stone, D. Convey, N. Neithalath, Pore- and micro-structural characterization of a novel structural binder based on iron carbonation, *Mater. Charact.* 98 (2014) 168–179.

- [23] S. Das, A. Hendrix, D. Stone, N. Neithalath, Flexural fracture response of a novel iron carbonate matrix – glass fiber composite and its comparison to Portland cement-based composites, *Constr. Build. Mater.* 93 (2015) 360–370.
- [24] R. Sarshar, G.A. Khoury, Material and environmental factors influencing the compressive strength of unsealed cement paste and concrete at high temperatures, *Mag. Concr. Res.* 45 (1993) 51–61.
- [25] C. Alonso, L. Fernandez, Dehydration and rehydration processes of cement paste exposed to high temperature environments, *J. Mater. Sci.* 39 (2004) 3015–3024.
- [26] W.P.S. Dias, G.A. Khoury, P.J.E. Sullivan, Mechanical properties of hardened cement paste exposed to temperatures up to 700 °C (1292 °F), *ACI Mater. J.* 87 (1990).
- [27] H.Y. Moon, H.S. Kim, D.S. Choi, Relationship between average pore diameter and chloride diffusivity in various concretes, *Constr. Build. Mater.* 20 (2006) 725–732.
- [28] E. Ghafari, H. Costa, E. Júlio, A. Portugal, L. Durães, The effect of nanosilica addition on flowability, strength and transport properties of ultra high performance concrete, *Mater. Des.* 59 (2014) 1–9.
- [29] V.M. Sánchez-Fajardo, M.E. Torres, A.J. Moreno, Study of the pore structure of the lightweight concrete block with lapilli as an aggregate to predict the liquid permeability by dielectric spectroscopy, *Constr. Build. Mater.* 53 (2014) 225–234.
- [30] S. Diamond, Mercury porosimetry: an inappropriate method for the measurement of pore size distributions in cement-based materials, *Cem. Concr. Res.* 30 (2000) 1517–1525, [http://dx.doi.org/10.1016/S0008-8846\(00\)00370-7](http://dx.doi.org/10.1016/S0008-8846(00)00370-7).
- [31] F. Moro, H. Böhni, Ink-bottle effect in mercury intrusion porosimetry of cement-based materials, *J. Colloid Interface Sci.* 246 (2002) 135–149.
- [32] PANalytical BV, X'Pert HighScore Plus Software, Version 2.2 b. Almelo Neth, 2006.
- [33] L.V. Olysysh, M.F. Vigasina, L.V. Melchakova, L.P. Ogorodova, I.V. Pekov, N.V. Chukanov, Thermal evolution and thermochemistry of the cancrinite-group carbonate–oxalate mineral, *Geochem. Int.* 49 (2011) 731–737.
- [34] W.A. Deer, Rock-forming minerals: non-silicates, volume 5B, *Geol. Soc. Lond.* (1998).
- [35] Li X-G, Lv Y, Ma B-G, Wang W-Q, Jian S-W. Decomposition kinetic characteristics of calcium carbonate containing organic acids by TGA. *Arab. J. Chem.* doi:<http://dx.doi.org/10.1016/j.arabjc.2013.09.026>.
- [36] Q. Qingjie, M. Yundong, L.I.U. Jian-zhong, C. Xinyu, C. Kefa, Thermo-gravimetric experiment research on thermal decomposition mechanics of calcium carbonate, *J. Liaoning Tech. Univ.* 21 (2002) 689–692.
- [37] B.C. Smith, *Infrared Spectral Interpretation: A Systematic Approach*, CRC press, 1998.
- [38] F.A. Miller, C.H. Wilkins, Infrared spectra and characteristic frequencies of inorganic ions, *Anal. Chem.* 24 (1952) 1253–1294.
- [39] P. Rovnaník, P. Bayer, P. Rovnaníková, Characterization of alkali activated slag paste after exposure to high temperatures, *Constr. Build. Mater.* 47 (2013) 1479–1487.
- [40] Z. Zhang, H. Wang, J.L. Provis, F. Bullen, A. Reid, Y. Zhu, Quantitative kinetic and structural analysis of geopolymers. Part 1. The activation of metakaolin with sodium hydroxide, *Thermochim. Acta* 539 (2012) 23–33.
- [41] S. Savoye, L. Legrand, G. Sagon, S. Lecomte, A. Chausse, R. Messina, et al., Experimental investigations on iron corrosion products formed in bicarbonate/carbonate-containing solutions at 90 °C, *Corros. Sci.* 43 (2001) 2049–2064.
- [42] D. Dimas, I. Giannopoulou, D. Panias, Polymerization in sodium silicate solutions: a fundamental process in geopolymerization technology, *J. Mater. Sci.* 44 (2009) 3719–3730.
- [43] D. Eniu, C. Gruian, E. Vanea, L. Patcas, V. Simon, FTIR and EPR spectroscopic investigation of calcium-silicate glasses with iron and dysprosium, *J. Mol. Struct.* 1084 (2015) 23–27.
- [44] A.M. Kozioł, Experimental determination of siderite (iron carbonate) stability under moderate pressure–temperature conditions, and application to Martian carbonate parageneses, *Lunar Planet. Sci. Conf.* 30 (1999) 1226.
- [45] A.M. Jubb, H.C. Allen, Vibrational spectroscopic characterization of hematite, maghemite, and magnetite thin films produced by vapor deposition, *ACS Appl. Mater. Interfaces* 2 (2010) 2804–2812.
- [46] H. Lepp, Stages in the Oxidation of Magnetite, vol. 42 *Mineralogical Soc Amer*, 1015 Eighteenth St, NW Suite 601, Washington, DC 20036, 1957.
- [47] M.I. Dar, S.A. Shivashankar, Single crystalline magnetite, maghemite, and hematite nanoparticles with rich coercivity, *RSC Adv.* 4 (2014) 4105–4113.
- [48] P.N.W. Verhoef, J.P.J.V. Dalen, Chemical and mechanical stability of hematite iron-ore in seawater, *Bull. Int. Assoc. Eng. Geol.-Bull. Assoc. Int. Géol. Ing.* 28 (1983) 233–239.
- [49] A.S. Teja, P.-Y. Koh, Synthesis, properties, and applications of magnetic iron oxide nanoparticles, *Prog. Cryst. Growth Charact. Mater.* 55 (2009) 22–45.
- [50] J. Rouquerol, D. Avnir, C.W. Fairbridge, D.H. Everett, J.M. Haynes, N. Pernicone, et al., Recommendations for the characterization of porous solids (technical report), *Pure Appl. Chem.* 66 (1994) 1739–1758.
- [51] N.V.Y. Scarlett, M.I. Pownceby, I.C. Madsen, A.N. Christensen, Reaction sequences in the formation of silico-ferrites of calcium and aluminum in iron ore sinter, *Metall. Mater. Trans. B Process Metall. Mater. Process. Sci.* 35 (2004) 929–936.
- [52] A.M. Neville, *Properties of Concrete*, 4th and final ed., 1995.
- [53] P.K. Mehta, P.J. Monteiro, *Concrete: Microstructure, Properties, and Materials*, vol. 3 McGraw-Hill, New York, 2006.
- [54] U. Schneider, Concrete at high temperatures – a general review, *Fire Saf. J.* 13 (1988) 55–68.
- [55] A.-Ç. Özge, Ç. Oğuzhan, R. Kambiz, Effect of high temperature on mechanical and microstructural properties of cement mortar, 11DBMC Int. Conf. Durab. Build. Mater. Compon. Istanbul, Turkey 2008, pp. 11–14.
- [56] S.Y.N. Chan, G.-F. Peng, M. Anson, Fire behavior of high-performance concrete made with silica fume at various moisture contents, *ACI Mater. J.* 96 (1999).